



You have downloaded a document from  
**RE-BUS**  
repository of the University of Silesia in Katowice

**Title:** Combustion synthesis, structural, magnetic and dielectric properties of Gd<sup>3+</sup>-doped lead molybdate–tungstates

**Author:** Tadeusz Groń, Monika Oboz, Bogdan Sawicki, Sebastian Pawlus, Andrzej Nowok, Zenon Kukuła i in.

**Citation style:** Groń Tadeusz, Oboz Monika, Sawicki Bogdan, Pawlus Sebastian, Nowok Andrzej, Kukuła Zenon i in . (2020). Combustion synthesis, structural, magnetic and dielectric properties of Gd<sup>3+</sup>-doped lead molybdate–tungstates. "Journal of Advanced Ceramics" Vol. 9, iss. 2 (2020), s. 255-268, doi 10.1007/s40145-020-0366-9



Uznanie autorstwa - Licencja ta pozwala na kopiowanie, zmienianie, rozprowadzanie, przedstawianie i wykonywanie utworu jedynie pod warunkiem oznaczenia autorstwa.



UNIwersytet ŚLĄSKI  
W KATOWICACH



Biblioteka  
Uniwersytetu Śląskiego



Ministerstwo Nauki  
i Szkolnictwa Wyższego

# Combustion synthesis, structural, magnetic and dielectric properties of Gd<sup>3+</sup>-doped lead molybdate–tungstates

T. GRON<sup>a</sup>, M. MACIEJKOWICZ<sup>b</sup>, E. TOMASZEWICZ<sup>b,\*</sup>, M. GUZIK<sup>c</sup>,  
M. OBOZ<sup>a</sup>, B. SAWICKI<sup>a</sup>, S. PAWLUS<sup>a</sup>, A. NOWOK<sup>a</sup>, Z. KUKUŁA<sup>a</sup>

<sup>a</sup>Institute of Physics, University of Silesia, 40-007 Katowice, Poland

<sup>b</sup>Faculty of Chemical Technology and Engineering, Department of Inorganic and Analytical Chemistry,  
West Pomeranian University of Technology in Szczecin, Al. Piastów 42, 71-065 Szczecin, Poland

<sup>c</sup>Faculty of Chemistry, University of Wrocław, ul. F. Joliot-Curie 14, 50-383 Wrocław, Poland

Received: October 28, 2019; Revised: January 24, 2020; Accepted: February 9, 2020

© The Author(s) 2020.

**Abstract:** Gd<sup>3+</sup>-doped lead molybdate–tungstates with the chemical formula of Pb<sub>1-3x</sub>□<sub>x</sub>Gd<sub>2x</sub>(MoO<sub>4</sub>)<sub>1-3x</sub>(WO<sub>4</sub>)<sub>3x</sub> (where  $x = 0.0455, 0.0839, 0.1430$ , corresponding to 9.53, 18.32, 33.37 mol% of Gd<sup>3+</sup>, respectively, as well as □ denotes cationic vacancies) were successfully synthesized via combustion route. The XRD and SEM results confirmed the formation of single-phase, tetragonal scheelite-type materials (space group  $I4_1/a$ ) with the uniform, spherical and oval grains ranging from 5 to 20 μm. Individual grains are strongly agglomerated into big clusters with the size even above 50 μm. The magnetic measurements as well as the Brillouin fitting procedure showed paramagnetic state with characteristic superparamagnetic-like behaviour and the short-range ferromagnetic interactions. The electrical and broadband dielectric spectroscopy studies revealed insulating properties with the residual electrical  $n$ -type conduction of  $2 \times 10^{-9}$  S/m and low energy loss ( $\tan \delta \approx 0.01$ ) below 300 K. Dielectric analysis showed that no dipole relaxation processes in the Gd<sup>3+</sup>-doped materials were observed. A fit of dielectric loss spectra of Gd<sup>3+</sup>-doped samples by sum of the conductivity and the Havriliak–Negami, Cole–Cole, and Cole–Davidson functions confirmed this effect.

**Keywords:** scheelite; Gd<sup>3+</sup>-substituted PbMoO<sub>4</sub>; combustion; solid solution; magnetic properties; dielectric properties

## 1 Introduction

Divalent metal molybdates and tungstates are an important and very wide group of inorganic materials that exhibit various interesting and functional properties.

Tetragonal scheelite-type crystals (space group  $I4_1/a$ ) with the chemical formula of ABO<sub>4</sub> (A = Ca, Sr, Ba, Pb; B = Mo or W; CdMoO<sub>4</sub>) both un-doped, as well as activated with RE<sup>3+</sup> ions are very interesting because of their excellent properties such as intense luminescence and main application as scintillators and photocatalysis [1–17]. Among them, lead molybdate (PbMoO<sub>4</sub>) is an important material due to its intense photoluminescence emission and simulated Raman scattering [10,14]. For

\* Corresponding author.

E-mail: tomela@zut.edu.pl

these reasons, lead molybdate is an excellent material for designing of radiation detection and scintillating devices [11–13]. However, even though the luminescent properties of  $\text{PbMoO}_4$  remains much investigated, its electrical properties and applications as dielectric material are not much explored.

Nowadays, inorganic materials containing rare earth ions (e.g.  $\text{La}^{3+}$ ) and magnetic transition metal ions (e.g.  $\text{Mn}^{2+}$ ) are at the top of electrical and magnetic research. In polycrystalline ceramics of  $\text{La}_{0.67}\text{Ca}_{0.33-x}\text{K}_x\text{MnO}_3$  (LCKMO) ( $x = 0.05, 0.10, 0.15, 0.20, \text{ and } 0.25$ ) and  $\text{La}_{0.7}\text{Ca}_{0.3-x}\text{K}_x\text{MnO}_3$  ( $x = 0, 0.01, 0.02, 0.03, \text{ and } 0.04$ ) prepared by sol–gel method, the insulator–metal (I–M) transition temperature was shifted to higher temperature and the temperature coefficient of resistivity decreased sharply with the substitution of  $\text{Ca}^{2+}$  with  $\text{K}^+$  ions as well as the temperature dependence of magnetization showed that Curie temperature was increasing with the increase of  $\text{K}^+$  content [18,19]. Insightful analysis of data showed that magnetoresistance was affected by  $\text{K}^+$  substitution [19]. In the same LCKMO ceramics ( $x = 0, 0.01, 0.03, 0.05, 0.10$ ) doped with  $\text{Sm}_2\text{O}_3$ , the temperature dependence of resistivity showed a double I–M transition for  $x \geq 0.03$  and a single I–M one for  $x \geq 0.05$  with broad transition width at low temperature. Effects of  $\text{Sm}_2\text{O}_3$ -adding showed the enhanced transversal low-field magnetoresistance at low applied magnetic field of 300 and 500 mT over a broad temperature range of below  $\sim 260$  K [20].

Our studies on electrical and magnetic properties of new tungstates [21–28], molybdates [29–31], and molybdate–tungstates [28,32,33] doped with rare earth ions ( $\text{RE}^{3+}$ ) and obtained both in the form of nano-, micropowders, and single crystals have shown that they are non-conductive paramagnetics or superparamagnetics. The reason for this is the strong electron screening on  $4f$ -shells. In turn, dielectric spectroscopy studies have shown that these new materials containing additionally  $d$ -electron metal ions with unfilled  $3d$ -shells have a bigger capacity for charge accumulation, which is usually accompanied by bigger energy loss [22,23]. Among the paramagnetic rare earth ions, gadolinium ion ( $\text{Gd}^{3+}$ ,  $4f^7$ ) possesses a large magnetic moment due to its isotropic electronic ground state of  ${}^8S_{7/2}$ . Because of the excellent magnetic resonance imaging effect observed for  $\text{Gd}^{3+}$  ions they are used as a common MRI contrast agent [34–36].

Recently, we carried out magnetic and broadband dielectric spectroscopy measurements on samples of

$\text{Pb}_{1-3x}\square_x\text{Gd}_{2x}(\text{MoO}_4)_{1-3x}(\text{WO}_4)_{3x}$  solid solution ( $x = 0.0455, 0.0839, 0.1154, 0.1430, 0.1667, 0.1774$ ) obtained by solid state reaction method [33]. The results showed a paramagnetic state with characteristic superparamagnetic-like behaviour and an existence of the faster (for  $\text{Gd}^{3+}$ -poorer samples with  $x$  up to 0.1154) and slower (for  $\text{Gd}^{3+}$ -richer samples with  $x > 0.1154$ ) relaxation processes [33]. The slowing down of relaxation process was explained by the increase of sample density with increasing  $\text{Gd}^{3+}$  ion content. In the present work,  $\text{Pb}_{1-3x}\square_x\text{Gd}_{2x}(\text{MoO}_4)_{1-3x}(\text{WO}_4)_{3x}$  ( $x = 0.0455, 0.0839, 0.1430$ ) samples were successfully synthesized via a citrate–nitrate combustion method. Because this method allows to obtain grain sizes close to nanometers, we expect to obtain materials with low energy loss that could be potentially used in electronics and technology.

## 2 Experimental

### 2.1 Combustion synthesis

Samples of pure  $\text{PbMoO}_4$  and solid solution described by the chemical formula of  $\text{Pb}_{1-3x}\square_x\text{Gd}_{2x}(\text{MoO}_4)_{1-3x}(\text{WO}_4)_{3x}$  ( $x = 0.0455, 0.0839, 0.1430$ , where  $\square$  denotes cationic vacancies) were successfully obtained via combustion method. The following precursors with the purity min. 99.9% were used for this synthesis: gadolinium oxide ( $\text{Gd}_2\text{O}_3$ ), anhydrous lead nitrate ( $\text{Pb}(\text{NO}_3)_2$ ), hydrated ammonium molybdate ( $(\text{NH}_4)_6\text{Mo}_7\text{O}_{24} \cdot 1.36\text{H}_2\text{O}$ ), and hydrated ammonium tungstate ( $(\text{NH}_4)_{10}\text{H}_2\text{W}_{12}\text{O}_{42} \cdot 3.45\text{H}_2\text{O}$ ). The number of water molecules in Mo and W precursors was established precisely in DTA–TG measurements. Monohydrate citric acid ( $\text{C}_6\text{H}_8\text{O}_7 \cdot \text{H}_2\text{O}$ ) was applied as a fuel in a combustion synthesis.

At the first step, an adequate amount of  $\text{Gd}_2\text{O}_3$  (0.1673 g; 0.462 mmol for  $x = 0.0839$ ) was dissolved in hot aqueous solution of nitric acid (1:1). Then, stoichiometric amount of  $\text{Pb}(\text{NO}_3)_2$  (1.3637 g; 4.117 mmol for  $x = 0.0839$ ) and citric acid (2.3124 g; 11.004 mmol, two-fold molar excess in relation to the number of moles of the final product) were added to the solution containing  $\text{Gd}^{3+}$  ions. The pH of as-obtained solution (solution A) was adjusted to the value of  $\sim 5$  with an ammonia solution (1:1). Precursors of Mo (0.6989 g; 0.588 mmol for  $x = 0.0839$ ) and W (0.3604 g; 0.115 mmol for  $x = 0.0839$ ) were dissolved in hot and deionized water (solution B). Next, the solutions A and B were mixed together and gently heated to completely

evaporate of water. In the next stage, obtained yellow powder was heated carefully at 573 K and a highly exothermic combustion reaction took place. During this process, large amount of gases evolved and the temperature of each sample increased very fast. In the last step, the fluffy powder was calcined at 1173 K for 2 h in air to obtain the final cream colour product (~2 g, ~5.50 mmol when  $x = 0.0839$ ). The temperature of final calcination was determined by us on the literature information for combustion synthesis of other RE<sup>3+</sup>-doped scheelite-type tungstates, i.e. CaWO<sub>4</sub>:Ln<sup>3+</sup> (Ln = Tb, Dy, and Ho) [37], NaLu<sub>1-x</sub>Eu<sub>x</sub>(WO<sub>4</sub>)<sub>2</sub> [38], and our own experience in combustion synthesis of scheelite-type Mn<sup>2+</sup>-doped calcium molybdate–tungstates with the formula of Ca<sub>1-x</sub>Mn<sub>x</sub>(MoO<sub>4</sub>)<sub>0.50</sub>(WO<sub>4</sub>)<sub>0.50</sub> [39].

For chemical compatibility analysis of Pb<sub>1-3x</sub>Gd<sub>2x</sub>(MoO<sub>4</sub>)<sub>1-3x</sub>(WO<sub>4</sub>)<sub>3x</sub> materials with Ag and Al powder, 30 wt% Al and 30 wt% Ag (both metals with the purity of min. 99.9%, 4–7 μm, Alfa Aesar) were mixed with the Gd<sup>3+</sup>-doped material for  $x = 0.0839$  and heated at 873 K within 4 h. Furthermore, the Gd<sup>3+</sup>-doped sample mixed with Ag powder was also co-fired at sintered temperature, i.e. 1173 K within 4 h. The temperature of co-firing was chosen according to the melting point of Al (933 K) and Ag (1235 K).

## 2.2 Methods

Powder X-ray diffraction patterns of lead molybdate and Gd<sup>3+</sup>-doped samples were collected within the 10°–100° 2θ range with the scanning step of 0.013° and the count time of 10 s per step on an EMPYREAN II diffractometer (PANalytical) using Cu Kα<sub>1,2</sub> radiation (λ = 0.15418 nm). XRD patterns were analysed by a *HighScore Plus 4.0* as well as *POWDER* software [40,41].

Morphology and grain size of all materials as well as their elemental composition were examined using a Hitachi S-3400 N microscope and an energy dispersive X-ray spectroscopy Thermo Scientific Ultra Dry detector, respectively. The examined samples were coated with palladium–gold alloy thin film using thermal evaporation PVD method to provide electric conductivity.

The static DC magnetic susceptibility was measured within the temperature range of 2–300 K and in two different cooling modes. In the zero-field cooled (ZFC) mode, each sample was at the beginning cooled down in the absence of an external magnetic field and then it was investigated during heating in the magnetic field of  $H_{dc} = 1$  kOe. Field cooled (FC) mode usually followed by ZFC run when the same magnetic field was set on at

high temperatures and measurements were performed with decreasing temperature. Magnetization isotherms were recorded at 2, 10, 20, 40, 60, and 300 K using a Quantum Design MPMS-XL-7AC SQUID magnetometer in applied external fields up to 70 kOe. The effective magnetic moment was determined using the equation [42,43]:

$$\mu_{\text{eff}} = \sqrt{\frac{3k_{\text{B}}C}{N_{\text{A}}\mu_{\text{B}}^2}} \cong 2.828\sqrt{C}$$

where  $k_{\text{B}}$  is the Boltzmann constant,  $N_{\text{A}}$  is the Avogadro number,  $\mu_{\text{B}}$  is the Bohr magneton, and  $C$  is the molar Curie constant.

Electrical conductivity  $\sigma(T)$  of the samples under study was measured by the DC method using a KEITHLEY 6517B Electrometer/High Resistance Meter and within the temperature range of 76–400 K. The thermoelectric power  $S(T)$  was measured within the temperature range of 300–600 K with the help of a Seebeck Effect Measurement System (MMR Technologies, Inc., USA). Dielectric measurements were carried out on pellets of PbMoO<sub>4</sub> and Gd<sup>3+</sup>-doped materials which were polished as well as sputtered with (~80 nm) Ag electrodes. The studies were carried out in the frequency range from  $5 \times 10^2$  to  $1 \times 10^6$  Hz using a LCR HITESTER (HIOKI 3532-50, Japan) and within the temperature range of 80–400 K. For the electrical and dielectric measurements, the powder samples were compacted in a disc form (10 mm in diameter and 1–2 mm thick) using the pressure of 1.5 GPa within 5 min.

## 3 Results and discussion

### 3.1 Analysis of XRD and SEM results

#### 3.1.1 XRD of Pb<sub>1-3x</sub>Gd<sub>2x</sub>(MoO<sub>4</sub>)<sub>1-3x</sub>(WO<sub>4</sub>)<sub>3x</sub>

Figures 1(a) and 1(b) show the XRD patterns of pure PbMoO<sub>4</sub> and Pb<sub>1-3x</sub>Gd<sub>2x</sub>(MoO<sub>4</sub>)<sub>1-3x</sub>(WO<sub>4</sub>)<sub>3x</sub> ( $x = 0.0455, 0.0839, 0.1430$ ) powder sintered at 1173 K within 2 h. The diffraction patterns of all samples show crystalline nature of the materials. No additional phases were detected. This fact suggests the complete solubility of Gd<sup>3+</sup> and W<sup>6+</sup> in PbMoO<sub>4</sub> crystal lattice. All observed diffraction lines shifted towards higher 2θ position with simultaneously increasing of Gd<sup>3+</sup> and W<sup>6+</sup> contents in the matrix (Fig. 1(b)). They were successfully indexed to the pure tetragonal scheelite-type structure with space group  $I4_1/a$  (No. 88, PbMoO<sub>4</sub> JCPDS Card No. 01-078-3062). The calculated lattice parameters ( $a$  and  $c$ ) linearly decreased with increasing  $x$  parameter (Fig. 2).

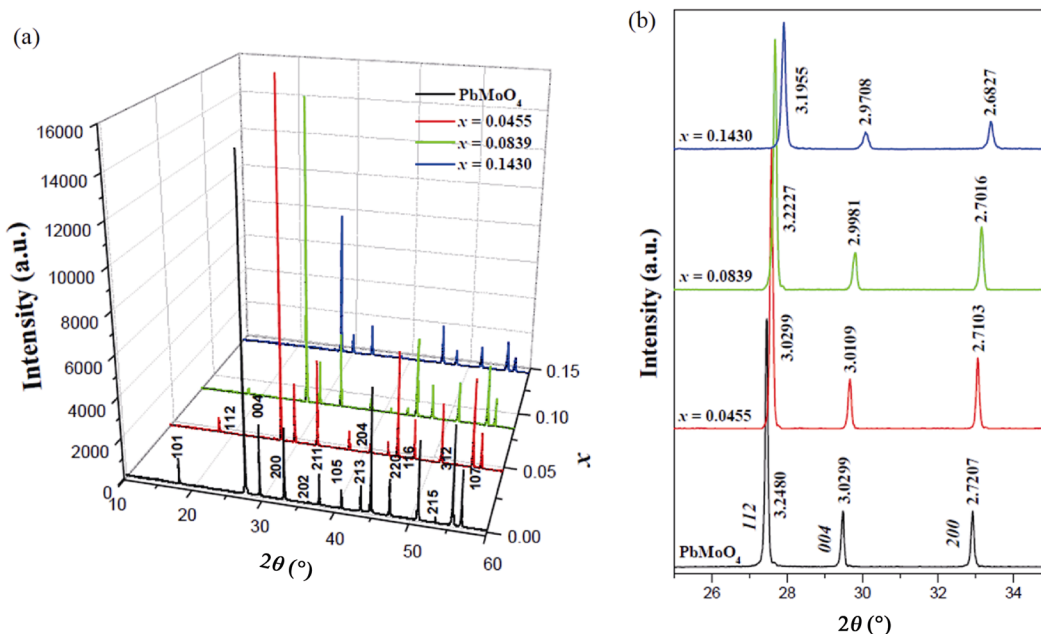


**Fig. 1** XRD patterns of  $\text{PbMoO}_4$  and  $\text{Pb}_{1-3x}\square_x\text{Gd}_{2x}(\text{MoO}_4)_{1-3x}(\text{WO}_4)_{3x}$  ( $x = 0.0455, 0.0839, 0.1430$ ) materials sintered at 1173 K within the range of  $2\theta$  from  $10^\circ$  to  $60^\circ$  (a) and the (112)/(004)/(200) diffraction peaks in the range of  $2\theta$  from  $25^\circ$  to  $35^\circ$  (b).

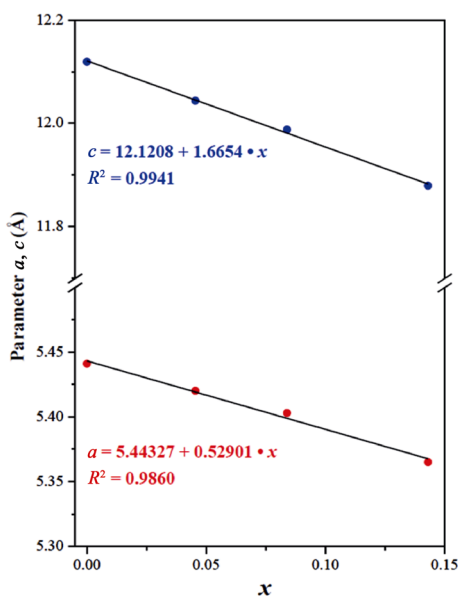


**Fig. 2** Linear dependence of both  $a$  and  $c$  lattice constants vs.  $x$  parameter.

It is because  $\text{Pb}^{2+}$  ions with the radius of  $1.29 \text{ \AA}$  (CN = 8) are substituted by significantly smaller  $\text{Gd}^{3+}$  ones ( $1.053 \text{ \AA}$  for CN = 8) [44]. The  $\text{Mo}^{6+}$  ions tetrahedrally coordinated by  $\text{O}^{2-}$  in  $\text{PbMoO}_4$  structure (ionic radius  $0.41 \text{ \AA}$ ) are substituted by only slightly bigger  $\text{W}^{6+}$  ones ( $0.42 \text{ \AA}$  for CN = 4) [44]. Thus, an introduction of  $\text{W}^{6+}$  ions into the matrix does not significantly change the lattice constants.

Figure 3 illustrates the XRD patterns of

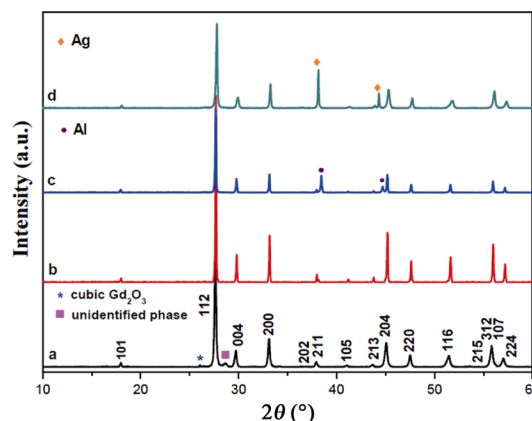


**Fig. 3** XRD patterns of  $\text{Pb}_{1-3x}\square_x\text{Gd}_{2x}(\text{MoO}_4)_{1-3x}(\text{WO}_4)_{3x}$  ( $x = 0.0839$ ) samples sintered at (a) 573 K, (b) 1173 K for 2 h, and co-fired materials with (c) 30 wt% Al and (d) 30% wt% Ag at 873 K for 4 h.

$\text{Pb}_{1-3x}\square_x\text{Gd}_{2x}(\text{MoO}_4)_{1-3x}(\text{WO}_4)_{3x}$  ( $x = 0.0839$ ) heated at 573 K (line a) and 1173 K (line b), respectively. The samples with various sintering temperature exhibited a difference in phase composition. At 573 K, some amounts of cubic  $\text{Gd}_2\text{O}_3$  and unidentified phase or phases perhaps arising from the partial decomposition of fuel or Mo/W precursors were detected. Our research (not presented here) showed also that heating of  $\text{Gd}^{3+}$ -doped material at temperatures higher than 573 K, i.e. at 673, 873, or 1073 K within 2 h did not allow the obtaining of pure scheelite-type material. No additional peaks were found in the diffraction pattern of sample

obtained after sintering at 1173 K, indicating that there were no other impurity phases in this material. It means that the pure scheelite-type material can be obtained by combustion route only if the final sintering temperature of each sample is relatively high and not less than 1173 K.

### 3.1.2 XRD and SEM of $Pb_{1-3x}Gd_{2x}(MoO_4)_{1-3x}(WO_4)_{3x}$ co-fired with Al and Ag

To evaluate the chemical compatibility with Al and Ag electrodes, 30 wt% of these metals were mixed with  $Pb_{1-3x}Gd_{2x}(MoO_4)_{1-3x}(WO_4)_{3x}$  sample for  $x = 0.0839$  and co-fired at 873 K within 4 h. The  $Gd^{3+}$ -doped sample mixed with Ag (30 wt%) was also co-fired at sintered temperature (1173 K). X-ray diffraction patterns of co-fired at 873 K materials with Al and Ag are presented in Fig. 3 (line c and line d). In turn, the backscattered electron images (BSE) and related energy-dispersive X-ray spectroscopy (EDS) analysis of the samples co-fired at 873 K are presented in Figs. 4(a) (Al) and 4(b) (Ag), respectively. Only the diffraction lines of  $Gd^{3+}$ -doped scheelite-type material and Al (JCPDS Card No. 04-016-2981) (violet circles located at Al peaks) or Ag (JCPDS Card No. 04-016-1389) (orange squares located at Ag peaks) were observed in the XRD patterns, implying that  $Pb_{1-3x}Gd_{2x}(MoO_4)_{1-3x}(WO_4)_{3x}$  samples did not react with Al and Ag powder at 873 K. XRD analysis (not presented here) of  $Gd^{3+}$ -doped material mixed with Ag and heated at sintered temperature showed

that this sample contained only two solid phases, i.e. scheelite-type powder and silver. This means that  $Gd^{3+}$ -doped lead molybdate–tungstates do not react with metallic Ag also at 1173 K. Only two types of grains with different grain sizes and distinct element contrast can be clearly distinguished in BSE images. The EDS analysis of co-fired sample with metallic aluminium (Fig. 4(a), area bounded by a yellow circle) revealed that the mainly existing element was Al (black grains). The presence of Pb, Gd, W, Mo, and O has also been reported (gray grains). The EDS results of co-fired scheelite-type sample with Ag (Fig. 4(b), area bounded by a yellow circle) revealed that the black area is silver grains and the emerald area is  $Gd^{3+}$ -doped material. Both EDS spectra contain also Au and Pd peaks. Their presence is due to the fact that the examined samples in the form of small discs were covered with Au and Pd alloy. These above facts clearly confirm that  $Gd^{3+}$ -doped lead molybdate–tungstates are chemically compatible with Al and Ag electrodes.

### 3.1.3 SEM of $Pb_{1-3x}Gd_{2x}(MoO_4)_{1-3x}(WO_4)_{3x}$

Morphology, microstructure, particle size, and chemical composition of all samples, i.e. un-doped lead molybdate as well as  $Gd^{3+}$ -doped lead molybdate–tungstates were analysed by scanning electron microscopy. The SEM micrographs are shown in Figs. 5(a)–5(h). Both pure lead molybdate as well as all doped samples are composed of spherical or oval grains with well-defined

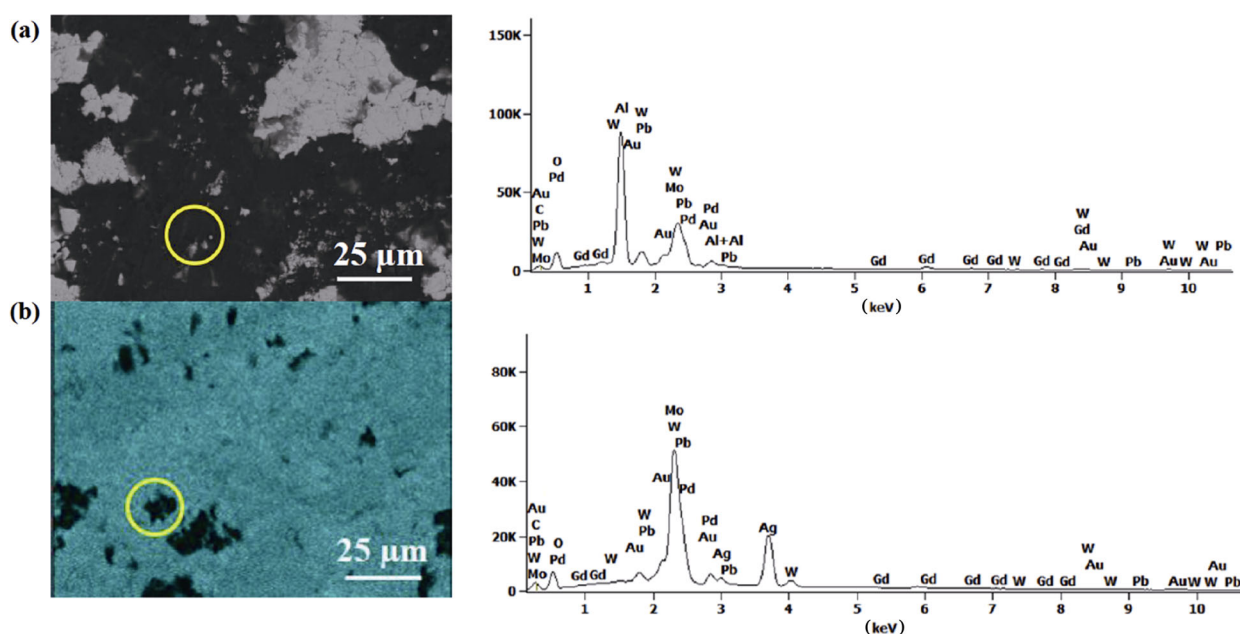


**Fig. 4** BSE micrographs and EDS spectra of  $Gd^{3+}$ -doped samples ( $x = 0.0839$ ) mixed with (a) 30 wt% Al (black grains—Al; gray grains— $Gd^{3+}$ -doped sample), (b) 30 wt% Ag (black grains—Ag; emerald grains— $Gd^{3+}$ -doped sample) and co-fired at 873 K.

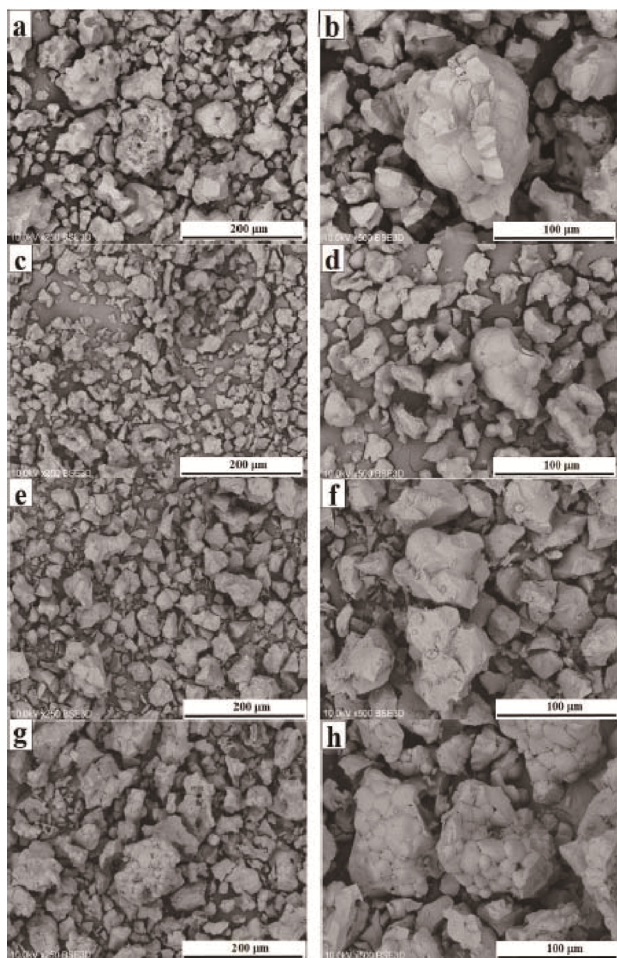


**Fig. 5** SEM micrographs of  $\text{PbMoO}_4$  (a, b) and  $\text{Pb}_{1-3x}\text{Gd}_{2x}(\text{MoO}_4)_{1-3x}(\text{WO}_4)_{3x}$  materials obtained by combustion route for  $x = 0.0455$  (c, d),  $x = 0.0839$  (e, f),  $x = 0.1430$  (g, h).

and sharp boundaries. It means that all obtained materials are well-crystallized. Regardless of a sample (pure matrix or doped material), the average size of an individual grain is in the range of about 5–20  $\mu\text{m}$ . However, we can find a number of grains with the size clearly below 1  $\mu\text{m}$ . Un-doped lead molybdate (Figs. 5(a) and 5(b)) is composed of particles which are agglomerated in small degree and form bigger clusters. Occasionally, it is possible to find groups of jointed particles with the size of up to about 50  $\mu\text{m}$ . The number of bigger clusters is increasing when the concentration of  $\text{Gd}^{3+}$  ions increased in the  $\text{Pb}_{1-3x}\text{Gd}_{2x}(\text{MoO}_4)_{1-3x}(\text{WO}_4)_{3x}$  materials (Figs. 5(c)–5(h)). The samples richer in  $\text{Gd}^{3+}$  ions, particularly the material for  $x = 0.1430$ , are composed of significant number of clusters. Some agglomerates reach the size over 50  $\mu\text{m}$ .

Usually, such big grains are not obtained by combustion method. Scheelite-type tungstates such as

$\text{CaWO}_4$  or  $\text{NaLu}(\text{WO}_4)_2$  doped with  $\text{RE}^{3+}$  ions obtained by a combustion route when a final calcination occurred at 1073 or 1173 K within 2 h contained individual particles with the size up to 100 nm [37,38]. Probably, the main reason of a rapid grain growth of  $\text{Pb}_{1-3x}\text{Gd}_{2x}(\text{MoO}_4)_{1-3x}(\text{WO}_4)_{3x}$  materials is their relatively low melting point and resulting small temperature difference between calcination process and melting. As we showed in our previous work, pure  $\text{PbMoO}_4$  obtained by solid state reaction method melts congruently at 1323 K [28,45].  $\text{Gd}^{3+}$ -doped lead molybdate–tungstates obtained by the same manner melt at lower temperatures, i.e. at 1315 K ( $x = 0.0455$ ), 1293 K ( $x = 0.0839$ ), and at 1279 K ( $x = 0.1430$ ) [28]. It means that this temperature difference is in the range of 106–150 K. Rapid grain growth during calcination was not observed with other doped scheelite-type matrices, e.g.  $\text{CaWO}_4$  (melting point 1863 K [39]). Sadeh *et al.* [37] obtained  $\text{CaWO}_4:\text{Ln}^{3+}$  ( $\text{Ln} = \text{Tb}, \text{Dy}, \text{Ho}$ ) nanomaterials by combustion method with the average grain size about 50 nm. In this case the temperature difference between calcination process and melting point of pure calcium tungstate is 690 K [37]. At this point, we should mention that  $\text{Pb}_{1-3x}\text{Gd}_{2x}(\text{MoO}_4)_{1-3x}(\text{WO}_4)_{3x}$  materials with the same  $\text{Gd}^{3+}$  ions concentration but obtained by traditional high-temperature solid state reaction route contained clearly bigger individual particles with the average size ranging from 20 to 70  $\mu\text{m}$ . Individual grains were also agglomerated to form very big clusters. The morphology of these materials was described precisely in our previous paper [33].

The EDX analysis results (not presented here) showed that only the elements which were present in the samples were Pb, Mo, and O (pure  $\text{PbMoO}_4$ ) or Pb, Mo, W, Gd, and O for  $\text{Gd}^{3+}$ -doped lead molybdate–tungstates. No peaks of any contaminations, especially organic carbon, were detected suggesting the high purity of each obtained sample. In addition, all identified elements were evenly distributed throughout the surface of each sample indicating a uniform chemical composition of each as-prepared material.

### 3.2 Magnetic properties

The results of magnetic susceptibility measurements of the  $\text{Pb}_{1-3x}\text{Gd}_{2x}(\text{MoO}_4)_{1-3x}(\text{WO}_4)_{3x}$  ( $x = 0.0455, 0.0839, 0.1430$ ) are depicted in Table 1 and Fig. 6(a). All studied mixed molybdate–tungstates are paramagnetic within the temperature range of 2–300 K and exhibit

**Table 1** Magnetic parameters of the  $\text{Pb}_{1-3x}\text{Gd}_{2x}(\text{MoO}_4)_{1-3x}(\text{WO}_4)_{3x}$  nanoparticles:  $C$  is the Curie constant,  $\theta$  is the Curie–Weiss temperature,  $\mu_{\text{eff}}$  is the effective magnetic moment,  $M$  is the magnetization at 2 K and in the magnetic field of 70 kOe,  $p_{\text{eff}}$  is the effective number of Bohr magnetons,  $M_0$  is the magnetization at the highest value of  $H/T$ , and  $g$  is the Landé factor

$x$	$C$ (emu·K/mol)	$\theta$ (K)	$\mu_{\text{eff}}$ ( $\mu_{\text{B}}$ /f.u.)	$M_{2\text{K}}$ ( $\mu_{\text{B}}$ /f.u.)	$p_{\text{eff}}$	$M_0$ ( $\mu_{\text{B}}$ /f.u.)	$g$
	Experiment					Brillouin fit	
0.0455	2.421	2.08	2.342	0.65	2.394	0.650	1.98
0.0839	1.555	1.48	3.168	1.17	3.251	1.175	1.91
0.1430	2.220	1.14	4.214	2.05	4.245	2.048	1.88

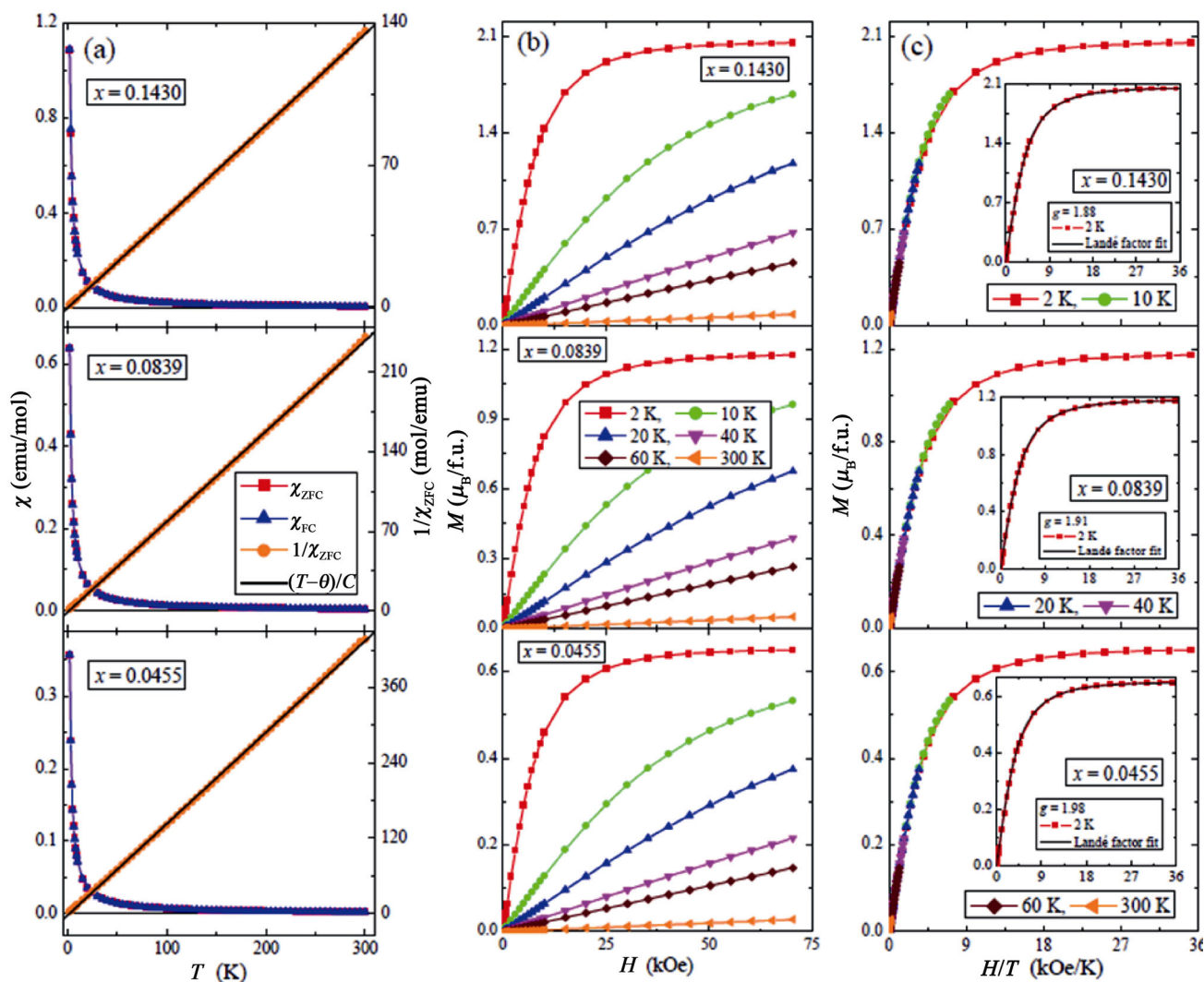


**Fig. 6** (a) ZFC and FC magnetic susceptibility  $\chi$  and  $1/\chi_{\text{ZFC}}$  vs. temperature  $T$  of  $\text{Pb}_{1-3x}\text{Gd}_{2x}(\text{MoO}_4)_{1-3x}(\text{WO}_4)_{3x}$  for  $x = 0.0455, 0.0839, 0.1430$  recorded at  $H = 1$  kOe. The solid (black) line,  $(T-\theta)/C$ , indicates a Curie–Weiss behaviour. (b) Magnetization  $M$  vs. temperature  $T$  of  $\text{Pb}_{1-3x}\text{Gd}_{2x}(\text{MoO}_4)_{1-3x}(\text{WO}_4)_{3x}$  for  $x = 0.0455, 0.0839, 0.1430$  at 2, 10, 20, 40, 60, and 300 K. (c) Magnetization  $M$  vs.  $H/T$  of  $\text{Pb}_{1-3x}\text{Gd}_{2x}(\text{MoO}_4)_{1-3x}(\text{WO}_4)_{3x}$  for  $x = 0.0455, 0.0839, 0.1430$  at 2, 10, 20, 40, 60, and 300 K. Inset: Landé factor fit (solid black line) to the experimental data at 2 K.

short-range ferromagnetic interactions visible in the positive values of Curie–Weiss temperature, that slightly decreases with increasing gadolinium ion content (Table 1). There was no splitting between the ZFC and

FC magnetic susceptibilities for any phase, which means no spin frustration as well as the absence of long-range magnetic interactions in the examined temperature range (Fig. 6(a)). The effective magnetic

moment,  $\mu_{\text{eff}}$ , is comparable to the effective number of Bohr magnetons,  $p_{\text{eff}}$ , for the  $\text{Gd}^{3+}$  ion with the effective spin of  $S = 7/2$ , given by the  $2[S(S+1)]^{1/2}$  expression [46]. This may mean that the  $\text{Gd}^{3+}$  ions carry only a spin magnetic moment.

The results of magnetic moment measurements of the materials under study are shown in Table 1 and Fig. 6(b). The shape of the magnetic isotherms shows saturation magnetization and no magnetic hysteresis are a consequence of the stable magnetization of a single domain particle. When the temperature was increasing their shape becomes linear, indicating paramagnetic response (Fig. 6(b)). In the reduced coordinate ( $H/T$ ) the magnetic isotherms fall exactly on a universal Brillouin curve for all samples under study (Fig. 6(c)). Such behaviour is characteristic of superparamagnetic particles. Similar behaviour was found by us in the following  $\text{RE}^{3+}$ -doped single crystals:  $\text{Cd}_{0.958}\text{Gd}_{0.028}\text{MoO}_4$  [30] and  $\text{Cd}_{0.9706}\text{Yb}_{0.0196}(\text{MoO}_4)_{0.9706}(\text{WO}_4)_{0.0294}$  [32] as well as in the microcrystalline materials such as:  $\text{ZnGd}_4\text{W}_3\text{O}_{16}$  [22],  $\text{Gd}_2\text{W}_2\text{O}_9$  [25], and  $\text{Pb}_{1-3x}\text{Gd}_{2x}(\text{MoO}_4)_{1-3x}(\text{WO}_4)_{3x}$  ( $x = 0.0455, 0.0839, 0.1154, 0.1430, 0.1667, 0.1774$ ) [33] obtained by high-temperature solid state reaction method. To investigate the nature of magnetism in the  $\text{Gd}^{3+}$ -doped materials obtained by combustion route, the Brillouin fitting procedure was applied [47]. The experimental virgin magnetization curves,  $M(H/T)$ , were fitted by the following expression:  $M(x) = M_0 B_J(x)$ , where  $M_0$  is the magnetization at the highest value of  $H/T$ ,  $x = gJ\mu_B H/k_B T$ ,  $g$  is the Landé factor, and  $B_J(x)$  is the standard Brillouin function. An effective angular momentum:  $J = S = 7/2$  of  $\text{Gd}^{3+}$  ions for all samples was assumed. The results of Brillouin fitting procedure depicted in the inset of Fig. 6(c) and in Table 1 showed a slight deviation of the Landé factor from  $g = 1.98$  for  $x = 0.0455$  to  $g = 1.88$  for  $x = 0.1430$ . This fact suggests that the orbital contribution to the magnetic moment slightly increases with the increasing of gadolinium ion content in the sample, giving some contribution to the spin–orbit coupling. The consequence of this may be a decrease in the ferromagnetic short-range interactions seen in the decreasing value of the paramagnetic Curie–Weiss temperature in the nonconductive  $\text{Gd}^{3+}$ -doped materials under study. One can conclude that the change of synthesis method and related reduction of grain size of  $\text{Gd}^{3+}$ -doped samples from 20–70  $\mu\text{m}$  [33] to 5–20  $\mu\text{m}$  (presented here) does not significantly affect the magnetic properties.

### 3.3 Electrical properties

The results of electrical measurements of  $\text{Pb}_{1-3x}\text{Gd}_{2x}(\text{MoO}_4)_{1-3x}(\text{WO}_4)_{3x}$  materials ( $x = 0.0455, 0.0839, 0.1430$ ) showed insulating behaviour with small values of the n-type electrical conductivity of  $\sigma \approx 2 \times 10^{-9}$  S/m. Its value slightly increases as the temperature and gadolinium ion content increase in the sample (Fig. 7). No thermal activation of the current carriers was observed. Similar behaviour we have observed for the following  $\text{RE}^{3+}$ -doped tungstates or molybdates:  $\text{R}_2\text{WO}_6$  ( $\text{R} = \text{Nd}, \text{Sm}, \text{Eu}, \text{Gd}, \text{Dy}, \text{Ho}$ ) [21],  $\text{CdRE}_2\text{W}_2\text{O}_{10}$  ( $\text{RE} = \text{Y}, \text{Pr}, \text{Nd}, \text{Sm}, \text{Gd–Er}$ ) [23,24],  $\text{AgY}_{1-x}\text{Gd}_x(\text{WO}_4)_2$  ( $x = 0.005, 0.01, 0.025, 0.04, 0.10, 0.20, 1.00$ ) [27],  $\text{Cd}_{1-3x}\text{Gd}_{2x}\text{MoO}_4$  ( $0.0005 \leq x \leq 0.0455$ ) [27], and  $\text{RE}_2\text{W}_2\text{O}_9$  ( $\text{RE} = \text{Pr}, \text{Sm–Gd}$ ) [26]. The residual electrical conduction of the n-type in the molybdate–tungstates under study seems to be connected with the anionic vacancies. Another explanation may be related to the fact that in a state of thermal equilibrium structural defects ( $n$ ) are always present in the lattice even in the crystal which is ideal in other respects. A necessary condition for free energy minimalization gives:  $n \cong N \exp(-E_v/k_B T)$  for  $n \ll N$ , where  $N$  is the number of atoms in the crystal and  $E_v$  is the energy required to transfer the atom from the bulk of the crystal on its surface [47]. Determined by dilatometric and X-ray measurements, the concentration of lead vacancy at the melting point (in molar fraction) was less than or equal to  $1.5 \times 10^{-4}$ . The corresponding estimate for the formation energy,  $E_v$ , of a vacancy in lead was  $E_v \geq 0.53$  eV [47]. Low formation energy in lead and the screened 4f-shells of gadolinium ions

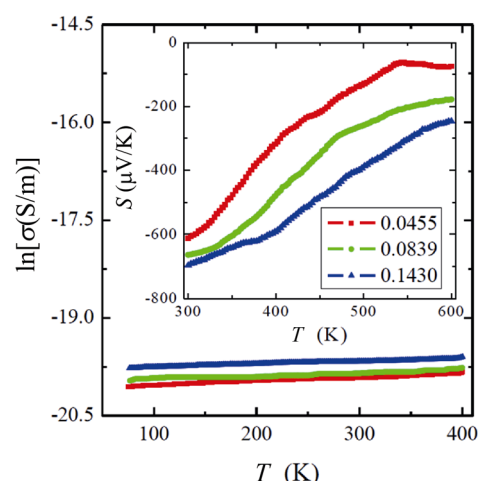


**Fig. 7** Electrical conductivity ( $\ln\sigma$ ) and thermoelectric power  $S$  (inset) vs. temperature  $T$  of  $\text{Pb}_{1-3x}\text{Gd}_{2x}(\text{MoO}_4)_{1-3x}(\text{WO}_4)_{3x}$  samples for  $x = 0.0455, 0.0839, 0.1430$ .

hinder the electron transport in the materials under study having an energy gap of more than 3 eV [28].

Dielectric spectroscopy studies of the samples with different concentration of  $Gd^{3+}$  ions revealed that these materials show some interesting electric properties, particularly low energy loss ( $\tan\delta \approx 0.01$ ) below 300 K. The temperature dependences of dielectric permittivity,  $\epsilon_r$ , and  $\tan\delta$  for various frequencies were similar for all doped materials and remain almost invariant on temperature changes up to ca. 300 K and 275 K for  $\epsilon_r$  and  $\tan\delta$ , respectively (Fig. 8). Further heating results in rapid increase of their values which becomes more pronounced when decreasing frequency. Moreover, even in the “plateau” region of  $\epsilon_r$  (or  $\tan\delta$ ), values of permittivity are slightly frequency-dependent. It has to be noticed that whereas the  $\epsilon_r$  parameter limits at low

temperatures to ca. 18.5 and 16.5 for materials with  $x = 0.0455$  and  $x = 0.0839$ , respectively (depending also on the measuring frequency), the low temperature limit of material with  $x = 0.1430$  is markedly lower, reaching the value of ca. 12.3. This difference becomes obvious from comparison of the  $\epsilon_r$  (100 kHz) spectra for all  $Gd^{3+}$  concentrations, as it was presented in Fig. 9.

### 3.4 Dielectric analysis

It has to be noticed that there are no signs of any dipole relaxation from the  $\epsilon_r$  (100 kHz) vs.  $T$  dependence in Fig. 9. However, at highest temperatures rise of  $\epsilon_r$  can suggest that some relaxation can exist for studied materials. To check if some dipole relaxation process in fact takes place in the materials under study, as it was previously observed for microcrystalline

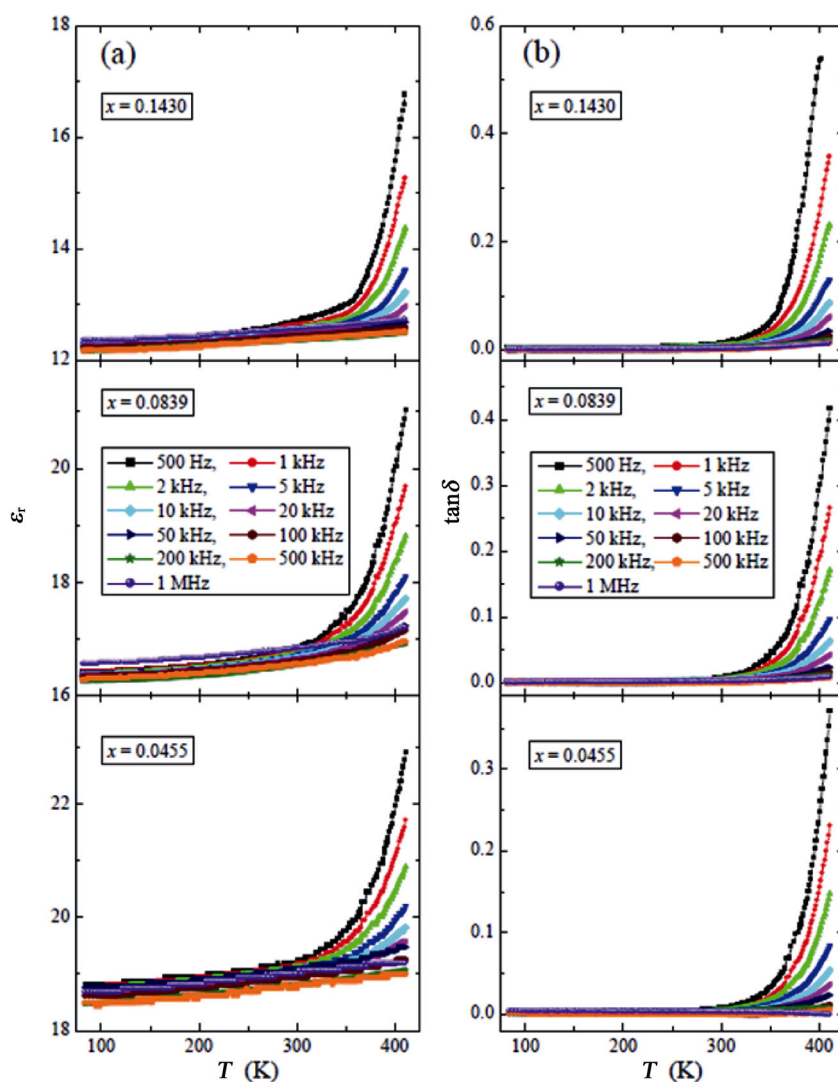


**Fig. 8** Relative permittivity  $\epsilon_r$  (a) and loss tangent  $\tan\delta$  (b) vs. temperature  $T$  within the frequency range of 500 Hz–1 MHz of  $Pb_{1-3x}\square_xGd_2(MoO_4)_{1-3x}(WO_4)_{3x}$  materials for  $x = 0.0455, 0.0839, 0.1430$ .

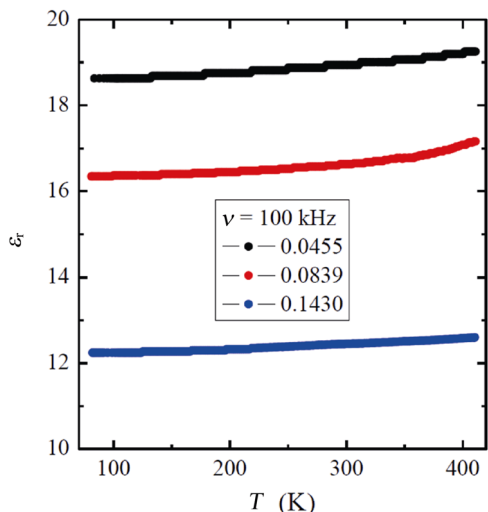


**Fig. 9** Temperature dependence of  $\epsilon_r$  at 100 kHz for  $Gd^{3+}$ -doped samples when  $x = 0.0455, 0.0839,$  and  $0.1430$ .

$Pb_{1-3x}□_xGd_{2x}(MoO_4)_{1-3x}(WO_4)_{3x}$  samples ( $x = 0.0455, 0.0839, 0.1154, 0.1430, 0.1667, 0.1774$ ) which were synthesized via solid state reaction route (SSR) [33], the dielectric data of the  $Gd^{3+}$ -doped materials obtained by combustion route were transformed to the frequency representation. In this representation analysis of the possible relaxation processes is much more precise than for the temperature representation. Figure 10 depicts frequency dependences of the dielectric permittivity,  $\epsilon'(ν)$ , and dielectric loss,  $\epsilon''(ν)$ , for all studied samples for representative temperatures. Contrary to the results presented in our previous paper [33] no dipole relaxation

processes were discerned on the spectra of the studied materials. To confirm this statement, spectra collected at the same temperature of 248 K for all samples obtained by combustion method were compared with the data collected at the same temperature for materials synthesized via solid state reaction route (SSR) and presented in Fig. 11(a). Whereas for the samples received by SSR route two relaxation processes are clearly visible, indicated by arrows, for the samples with smaller grains (combustion synthesis) there is no visible relaxation for this temperature in the accessible frequency range. Close inspection of the dielectric loss spectra presented in Fig. 11 for samples received by different synthesis methods exhibits that for the materials received via combustion route not only relaxation process remains invisible but also amplitude of the loss data is markedly lower than for the doped samples with bigger grains (solid state reaction route).

To parameterize the relaxation process for the materials received via SSR route the dielectric loss ( $\epsilon''$ ) spectra were fitted by sum of the conductivity and the two Havriliak–Negami (HN) equations [48]:

$$\epsilon''(\omega) = \text{Im} \left( \epsilon_\infty + \sum_i \frac{\Delta\epsilon_i}{[1+(i\omega\tau_i)^\alpha]^\beta} \right) + \frac{\sigma_{DC}}{\epsilon_0\omega} \quad (1)$$

where  $\epsilon_\infty$  is the high-frequency dielectric constant,  $\Delta\epsilon_i$  is the dielectric strength,  $\tau_i$  is the dielectric relaxation time,  $\alpha$  and  $\beta$  are the shape parameters, and  $\sigma_{DC}$  is the DC conductivity. The fitting curve (red line

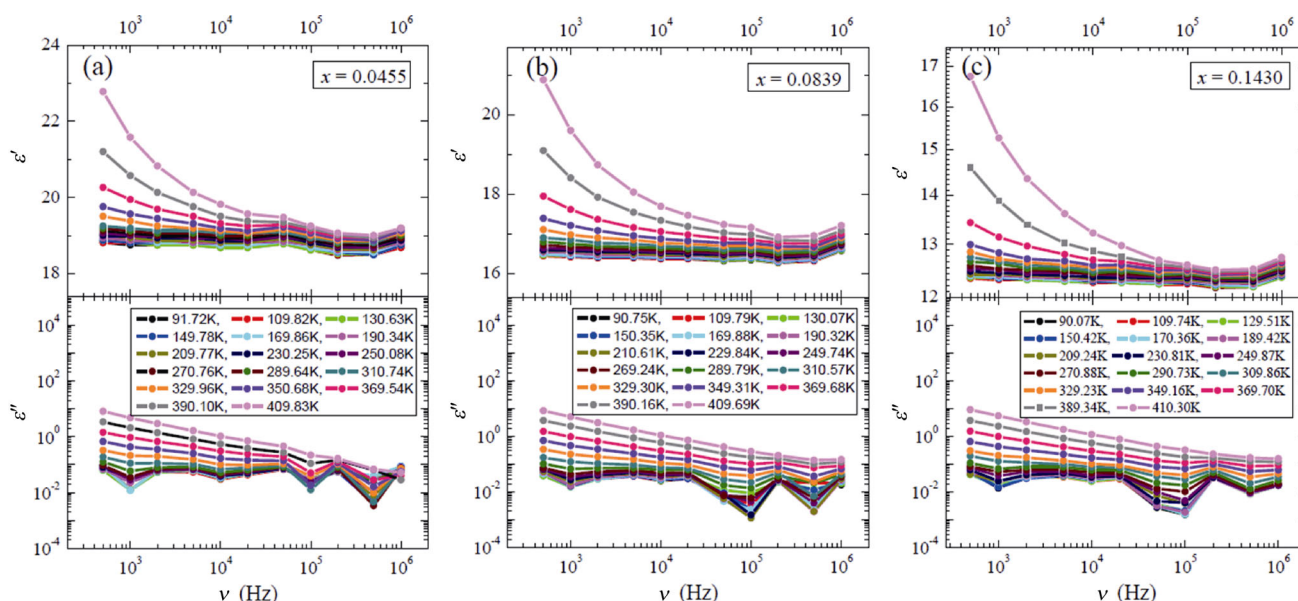


**Fig. 10** Representative  $\epsilon'(ν)$  and  $\epsilon''(ν)$  spectra for selected, the same temperatures and for  $Pb_{1-3x}□_xGd_{2x}(MoO_4)_{1-3x}(WO_4)_{3x}$  samples when (a)  $x = 0.0455,$  (b)  $x = 0.0839,$  and (c)  $x = 0.1430$ .

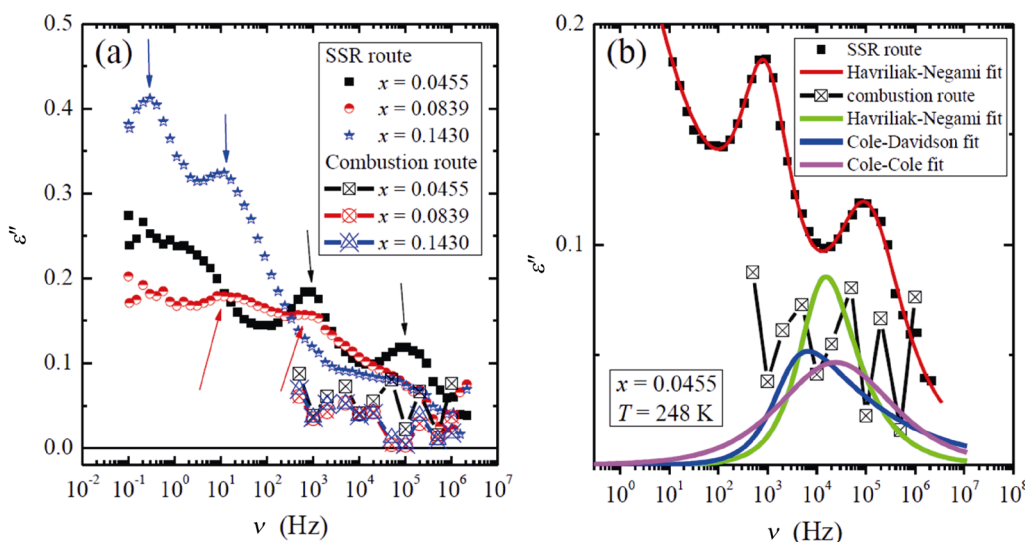


**Fig. 11** (a) Dependence of  $\epsilon''(\nu)$  at temperature of 248 K and different Gd<sup>3+</sup> concentrations for  $\text{Pb}_{1-3x}\text{Gd}_{2x}(\text{MoO}_4)_{1-3x}(\text{WO}_4)_{3x}$  samples synthesized via solid state reaction (SSR) route and via combustion method. Arrow indicates position of the relaxation processes. (b) Dependence of  $\epsilon''(\nu)$  at temperature of 248 K and concentration  $x = 0.0455$ , for samples synthesized via solid state reaction (SSR) method and via combustion route. Solid curves represent fits by various fitting functions used to parameterization of the relaxation processes.

in Fig. 11(b)) quite well describes the data. Instead of the very large scatter of the data points at 248 K measured for sample received via combustion route, the single Havriliak–Negami function was used to check the presumed relaxation process for the sample with  $x = 0.0455$ . The result of fitting procedure is presented in Fig. 11(b) as the green curve. The same data were also parameterized by the single Cole–Cole equation (i.e. Havriliak–Negami (HN) equation with fixed parameter  $\beta = 1$ , magenta curve in Fig. 11(b)) and by the single Cole–Davidson function (i.e. Havriliak–Negami equation with fixed parameter  $\alpha = 1$ , blue curve in Fig. 11(b)). As it can be deduced from the comparison of the three curves presented in Fig. 11(b), not only quality of these functions is very poor due to huge scatter of the fitted data points but also position of the maximum of hypothetical relaxation process is “model dependent”: dramatically depends on the choice of the fitting function. Consequently, it can be concluded that any reliable fitting procedure of the relaxation process or processes for samples received via combustion route remains impossible.

On the other hand, for all samples obtained by combustion method both  $\epsilon'$  and  $\epsilon''$  increase with decreasing of frequency. These two variables increase also during heating of samples. This behaviour might suggest that some dipole relaxation process can enter the experimental window at higher temperatures,

inaccessible in our experimental setup. It is worth emphasizing that  $\text{Pb}_{1-3x}\text{Gd}_{2x}(\text{MoO}_4)_{1-3x}(\text{WO}_4)_{3x}$  samples obtained by combustion method are accompanied by low energy loss up to room temperature. In other words, there is no dipole relaxation, and there is no energy loss. A similar phenomenon was observed for the  $\text{Pb}_{1-3x}\text{Gd}_{2x}(\text{MoO}_4)_{1-3x}(\text{WO}_4)_{3x}$  samples for the same Gd<sup>3+</sup> concentration but obtained by solid state reaction method [33]. It can be concluded that the appropriate grain size of the materials under study limit the freedom of electron charge or ionic. This behaviour is characteristic for the spatial charge polarization. Materials with such properties may have potential applications in electronics and technology.

The loss spectra,  $\epsilon''(\nu)$ , collected at two temperatures, i.e. at 140 K and 300 K ( $\pm 1$  K) for the samples under study were compared in Fig. 12. Dependences of  $\epsilon'(500 \text{ Hz})$  for the same two temperatures, i.e. 140 K and 300 K ( $\pm 1$  K) vs.  $x$  parameter are shown in Fig. 13. It is clear from these plots that  $\epsilon'$  decreases with  $x$  in linear manner. It can be also derived that whereas  $\epsilon'$  shows strong dependence on  $x$ , there is no correlation between  $\epsilon''$  and the concentration of Gd<sup>3+</sup> ions. As it has been already mentioned above, only slight increase of dielectric loss can be observed when the temperature was increasing, but there are no signs of any relaxation processes that emerge in the frequency window of the experiment in presented temperature range.

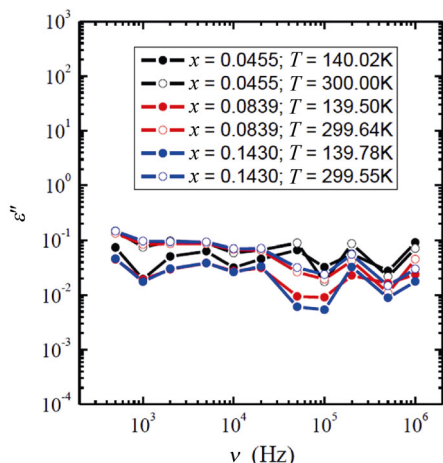


**Fig. 12** Dependence of  $\varepsilon''(\nu)$  at two temperatures, 140 K and 300 K ( $\pm 1$  K) and for different  $x$  parameter.

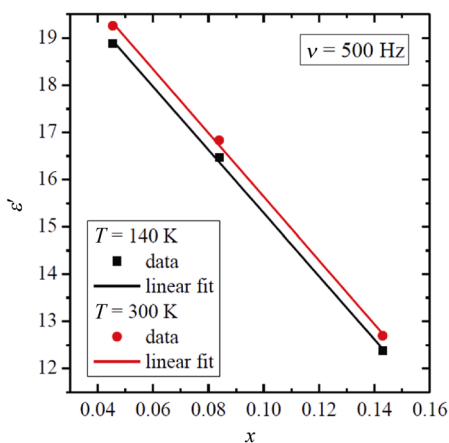


**Fig. 13** Dependence of  $\varepsilon'(500 \text{ Hz})$  on  $x$  at two temperatures, 140 K and 300 K ( $\pm 1$  K).

## 4 Conclusions

$\text{Gd}^{3+}$ -doped lead molybdate–tungstates with the chemical formula of  $\text{Pb}_{1-3x}\square_x\text{Gd}_{2x}(\text{MoO}_4)_{1-3x}(\text{WO}_4)_{3x}$  ( $x = 0.0455, 0.0839, 0.1430$ , where  $\square$  denotes cationic vacancies) were successfully obtained by a combustion method. The structural characterization showed formation of single phase scheelite-type tetragonal structure (space group  $I4_1/a$ ) at 1173 K without evidence of any secondary phases.  $\text{Gd}^{3+}$ -doped materials consist of uniform particles with an average size within the range of about 5–20  $\mu\text{m}$ . Individual grains join together to form bigger clusters with the size above 50  $\mu\text{m}$ . The number and size of clusters increase with increasing  $\text{Gd}^{3+}$  ion content in materials under study. Magnetic measurements and Brillouin fit procedure showed superparamagnetic-like behaviour with short-range

ferromagnetic interactions weakening with increasing of the orbital contribution to the magnetic moment as gadolinium ion content increased. Electrical measurements showed that  $\text{Gd}^{3+}$ -doped materials are the  $n$ -type insulators with small values of dielectric permittivity ( $\varepsilon_r \approx 20$ ) and loss tangent ( $\tan\delta \approx 0.01$ ) below room temperature. Dielectric analysis in the frequency representation showed that no dipole relaxation processes were discerned on  $\varepsilon'(\nu)$  and  $\varepsilon''(\nu)$  spectra. It means that the dipole relaxation disappears when the grain size decreases, causing the appearance of a spatial polarization, in which the freedom of electron charge or ionic is limited. And then the energy loss is smaller. This correlation has been additionally confirmed by the fit of dielectric loss spectra of  $\text{Pb}_{1-3x}\square_x\text{Gd}_{2x}(\text{MoO}_4)_{1-3x}(\text{WO}_4)_{3x}$  samples obtained by combustion as well as solid state reaction method of the same  $\text{Gd}^{3+}$  ions composition using the sum of conductivity and the Havriliak–Negami, Cole–Cole, and Cole–Davidson functions.

## Acknowledgements

This work was partly supported by Ministry of Science and Higher Education (Poland) and funded from Science Resources: No. 1S-0300–500-1-05-06 and UPB-DZS 518-10-020-3101-01/18. One of us (M. Maciejkowicz) would like to thank for the financial support from National Science Center of Poland for the grant PRELUDIUM 14 No. UMO-2017/27/N/ST8/00741.

## References

- [1] Danevich FA, Georgadze A, Kobychyev VV, *et al.* Application of  $\text{PbWO}_4$  crystal scintillators in experiment to search for decay of  $^{116}\text{Cd}$ . *Nucl Instrum Meth A* 2006, **556**: 259–265.
- [2] Annenkov AN, Auffray E, Chipaux R, *et al.* Systematic study of the short-term instability of  $\text{PbWO}_4$  scintillator parameters under irradiation. *Radiat Meas* 1998, **29**: 27–38.
- [3] Danevich FA, Kobychyev VV, Kobychyev RV, *et al.* Impact of geometry on light collection efficiency of scintillation detectors for cryogenic rare event searches. *Nucl Instrum Meth B* 2014, **336**: 26–30.
- [4] Korzhik MV, Kornoukhov VN, Missevitch OV, *et al.* Large volume  $\text{CaMoO}_4$  scintillation crystals. *IEEE T Nucl Sci* 2008, **55**: 1473–1475.
- [5] Nikl M, Boháček P, Mihóková E, *et al.* The doping of  $\text{PbWO}_4$  in shaping its scintillator characteristics. *Radiat Meas* 2001, **33**: 705–708.
- [6] Han ZF, Shi CS, Zhang GB, *et al.* Temperature dependence

- of  $\text{PbWO}_4$  scintillating. *J Electron Spectrosc* 1999, **101–103**: 583–585.
- [7] Belogurov S, Kornoukhov V, Annenkov A, *et al.*  $\text{CaMoO}_4$  scintillation crystal for the search of  $^{100}\text{Mo}$  double beta decay. *IEEE T Nucl Sci* 2005, **52**: 1131.
- [8] Xiong Y, Wang B, Zhuang H, *et al.* Doping-induced evolutions of  $\text{PbWO}_4$  mesocrystals and their optical properties. *RSC Adv* 2014, **4**: 36738–36741.
- [9] Xu W, Hu YW, Zheng LJ, *et al.* Enhanced NIR-NIR luminescence from  $\text{CaWO}_4:\text{Nd}^{3+}/\text{Yb}^{3+}$  phosphors by  $\text{Li}^+$  codoping for thermometry and optical heating. *J Lumin* 2019, **208**: 415–423.
- [10] Szczancoski JC, Bomio MDR, Cavalcante LS, *et al.* Morphology and blue photoluminescence emission of  $\text{PbMoO}_4$  processed in conventional hydrothermal. *J Phys Chem C* 2009, **113**: 5812–5822.
- [11] Danevich FA, Grinyov BV, Henry S, *et al.* Feasibility study of  $\text{PbWO}_4$  and  $\text{PbMoO}_4$  crystal scintillators for cryogenic rare events experiments. *Nucl Instrum Meth A* 2010, **622**: 608–613.
- [12] Nagornaya LL, Danevich FA, Dubovik AM, *et al.* Tungstate and molybdate scintillators to search for dark matter and double beta decay. *IEEE T Nucl Sci* 2009, **56**: 2513–2518.
- [13] Khan A, Daniel DJ, Kim H, *et al.* Luminescence and scintillation characterization of  $\text{PbMoO}_4$  crystal for neutrinoless double beta decay search. *Radiat Meas* 2019, **123**: 34–38.
- [14] Vyas A, Joshi CP, Moharil SV. NIR emitting phosphors based on  $\text{PbMoO}_4$  for modification of solar spectrum. *J Lumin* 2018, **196**: 259–263.
- [15] Xing GJ, Liu R, Zhao C, *et al.* Photoluminescence and photocatalytic properties of uniform  $\text{PbMoO}_4$  polyhedral crystals synthesized by microemulsion-based solvothermal method. *Ceram Int* 2011, **37**: 2951–2956.
- [16] Hernández-Uresti DB, Martínez-de la Cruz A, Aguilar-Garib JA. Photocatalytic activity of  $\text{PbMoO}_4$  molybdate synthesized by microwave method. *Catal Today* 2013, **212**: 70–74.
- [17] Hashim M, Hu CG, Wang X, *et al.* Synthesis and photocatalytic property of lead molybdate dendrites with exposed (001) facet. *Appl Surf Sci* 2012, **258**: 5858–5862.
- [18] Li D, Chen QM, Li ZY, *et al.* Structure, electrical and magnetic properties of  $\text{La}_{0.67}\text{Ca}_{0.33-x}\text{K}_x\text{MnO}_3$  polycrystalline ceramic. *J Mater Sci: Mater Electron* 2018, **29**: 1808–1816.
- [19] Li L, Zhang H, Liu X, *et al.* Structure and electromagnetic properties of  $\text{La}_{0.7}\text{Ca}_{0.3-x}\text{K}_x\text{MnO}_3$  polycrystalline ceramics. *Ceram Int* 2019, **45**: 10558–10564.
- [20] Li JF, Chen QM, Yang SA, *et al.* Electrical transport properties and enhanced broad-temperature-range low field magnetoresistance in LCMO ceramics by  $\text{Sm}_2\text{O}_3$  adding. *J Alloys Compd* 2019, **790**: 240–247.
- [21] Urbanowicz P, Tomaszewicz E, Groń T, *et al.* Magnetic properties of  $\text{R}_2\text{WO}_6$  (where  $\text{R}=\text{Nd}, \text{Sm}, \text{Eu}, \text{Gd}, \text{Dy}$  and  $\text{Ho}$ ). *Physica B* 2009, **404**: 2213–2217.
- [22] Urbanowicz P, Tomaszewicz E, Groń T, *et al.* Superparamagnetic-like behavior and spin–orbit coupling in  $(\text{Co},\text{Zn})\text{RE}_4\text{W}_3\text{O}_{16}$  tungstates ( $\text{RE}=\text{Nd}, \text{Sm}, \text{Eu}, \text{Gd}, \text{Dy}$  and  $\text{Ho}$ ). *J Phys Chem Solids* 2011, **72**: 891–898.
- [23] Kukula Z, Tomaszewicz E, Mazur S, *et al.* Dielectric and magnetic permittivities of three new ceramic tungstates  $\text{MPr}_2\text{W}_2\text{O}_{10}$  ( $\text{M}=\text{Cd}, \text{Co}, \text{Mn}$ ). *Philos Mag* 2012, **92**: 4167–4181.
- [24] Kukula Z, Tomaszewicz E, Mazur S, *et al.* Electrical and magnetic properties of  $\text{CdRE}_2\text{W}_2\text{O}_{10}$  tungstates ( $\text{RE}=\text{Y}, \text{Nd}, \text{Sm}, \text{Gd}-\text{Er}$ ). *J Phys Chem Solids* 2013, **74**: 86–93.
- [25] Mazur S, Tomaszewicz E, Groń T, *et al.* Paramagnetic behaviour in  $\text{RE}_2\text{W}_2\text{O}_9$  tungstates ( $\text{RE} = \text{Pr}, \text{Nd}, \text{Sm}-\text{Gd}$ ). *Solid State Phenom* 2012, **194**: 112–115.
- [26] Urbanowicz P, Piątkowska M, Sawicki B, *et al.* Dielectric properties of  $\text{RE}_2\text{W}_2\text{O}_9$  ( $\text{RE}=\text{Pr}, \text{Sm}-\text{Gd}$ ) ceramics. *J Eur Ceram Soc* 2015, **35**: 4189–4193.
- [27] Sawicki B, Groń T, Tomaszewicz E, *et al.* Some optical and transport properties of a new subclass of ceramic tungstates and molybdates. *Ceram Int* 2015, **41**: 13080–13089.
- [28] Piątkowska M, Fuks H, Tomaszewicz E, *et al.* New vacancies and  $\text{Gd}^{3+}$ -doped lead molybdate-tungstates and tungstates prepared via solid state and citrate-nitrate combustion method. *Ceram Int* 2017, **43**: 7839–7850.
- [29] Tomaszewicz E, Piątkowska M, Pawlikowska M, *et al.* New vacancies and  $\text{Dy}^{3+}$ -doped molybdates—Their structure, thermal stability, electrical and magnetic properties. *Ceram Int* 2016, **42**: 18357–18367.
- [30] Groń T, Tomaszewicz E, Berkowski M, *et al.* Dielectric and magnetic properties of  $\text{CdMoO}_4:\text{Gd}^{3+}$  single crystal. *J Alloys Compd* 2014, **593**: 230–234.
- [31] Groń T, Tomaszewicz E, Berkowski M, *et al.* Some optical, magnetic and transport properties of  $\text{CdMoO}_4:\text{Nd}^{3+}$ . *Ceram Int* 2016, **42**: 4185–4193.
- [32] Groń T, Tomaszewicz E, Berkowski M, *et al.*  $\text{Yb}^{3+}$ -doped cadmium molybdate-tungstate single crystal—Its structural, optical, magnetic and transport properties. *J Solid State Chem* 2018, **262**: 164–171.
- [33] Kukula Z, Maciejkowicz M, Tomaszewicz E, *et al.* Electric relaxation of superparamagnetic Gd-doped lead molybdate-tungstates. *Ceram Int* 2019, **45**: 4437–4447.
- [34] Sakai N, Zhu L, Kurokawa A, *et al.* Synthesis of  $\text{Gd}_2\text{O}_3$  nanoparticles for MRI contrast agents. *J Phys: Conf Ser* 2012, **352**: 012008.
- [35] Zhou ZJ, Huang DT, Bao JF, *et al.* A synergistically enhanced T1–T2 dual-modal contrast agent. *Adv Mater* 2012, **24**: 6223–6228.
- [36] Bae KH, Kim YB, Lee Y, *et al.* Bioinspired synthesis and characterization of gadolinium-labeled magnetite nanoparticles for dual contrast T1- and T2-weighted magnetic resonance imaging. *Bioconjugate Chem* 2010, **21**: 505–512.
- [37] Sadegh M, Badiei A, Abbasi A, *et al.* Preparation of  $\text{CaWO}_4:\text{Ln}^{3+}@/\text{SiO}_2$  ( $\text{Ln}=\text{Tb}, \text{Dy}$  and  $\text{Ho}$ ) nanoparticles by a combustion reaction and their optical properties. *J Lumin*

- 2010, **130**: 2072–2075.
- [38] Zhang D, Liu J, Pu X. Photoluminescence properties of  $\text{NaLu}_{1-x}\text{Eu}_x(\text{WO}_4)_2$  novel red phosphors synthesized by combustion method. *Frontier of Environmental Science* 2014, **3**: 1–5.
- [39] Pawlikowska M, Fuks H, Tomaszewicz E. Solid state and combustion synthesis of  $\text{Mn}^{2+}$ -doped scheelites—Their optical and magnetic properties. *Ceram Int* 2017, **43**: 14135–14145.
- [40] Taupin D. Une méthode générale pour l'indexation des diagrammes de poudres. *J Appl Cryst* 1968, **1**: 178–181.
- [41] Taupin D. A powder-diagram automatic-indexing routine. *J Appl Cryst* 1973, **6**: 380–385.
- [42] Groń T, Krok-Kowalski J, Duda H, *et al.* Metamagnetism in the  $\text{Cr}_2\text{V}_{4-x}\text{Mo}_x\text{O}_{13+0.5x}$  solid solutions. *Phys Rev B* 1995, **51**: 16021
- [43] Krok-Kowalski J, Groń T, Warczewski J, *et al.* Ferrimagnetism and metamagnetism in  $\text{Cd}_{1-x}\text{Cu}_x\text{Cr}_2\text{S}_4$  spinels. *J Magn Magn Mater* 1997, **168**: 129–138.
- [44] Shannon RD. Revised effective ionic radii and systematic studies of interatomic distances in halides and chalcogenides. *Acta Cryst A* 1976, **32**: 751–767.
- [45] Piątkowska M, Tomaszewicz E. Synthesis, structure, and thermal stability of new scheelite-type  $\text{Pb}_{1-3x}\text{Pr}_{2x}(\text{MoO}_4)_{1-3x}(\text{WO}_4)_{3x}$  ceramic materials. *J Therm Anal Calorim* 2016, **126**: 111–119.
- [46] Morrish AH. *Physical Principles of Magnetism*. New York: John Wiley & Sons, Inc., 1965.
- [47] Kittel C. *Introduction to Solid State Physics*. New York: John Wiley & Sons, Inc., 1971.
- [48] Havriliak S, Negami S. A complex plane representation of dielectric and mechanical relaxation processes in some polymers. *Polymer* 1967, **8**: 161–210.

**Open Access** This article is licensed under a Creative Commons Attribution 4.0 International License, which permits use, sharing, adaptation, distribution and reproduction in any medium or format, as long as you give appropriate credit to the original author(s) and the source, provide a link to the Creative Commons licence, and indicate if changes were made.

The images or other third party material in this article are included in the article's Creative Commons licence, unless indicated otherwise in a credit line to the material. If material is not included in the article's Creative Commons licence and your intended use is not permitted by statutory regulation or exceeds the permitted use, you will need to obtain permission directly from the copyright holder.

To view a copy of this licence, visit <http://creativecommons.org/licenses/by/4.0/>.